The influence of slope gradient and gully channel on the run-out behavior of rockslide-debris flow: an analysis on the Verghereto landslide in Italy

The influence of slope gradient and gully channel on the run-out behavior of rockslide-debris flow: an analysis on the Verghereto landslide in Italy

Wei Shen[1], Matteo Berti[1], Tonglu Li[2,3], Andrea Benini[4], Zhitian Qiao[1*]

*Correspondence author

1 Department of Biological, Geological and Environmental Sciences, University of Bologna, Italy, 40126

2 Department of Geological Engineering, Chang'an University, Xi'an, China, 710064

3 Water Cycle and Geological Environment Observation and Research Station for the Chinese Loess Plateau, Ministry of Education, Gansu China, 745399

4 Servizio Tecnico Bacino Romagna Regione Emilia-Romagna

Paper submitted to “Landslides” for review and possible publication

Abstract:

Rockslide-debris flow is a hybrid type of mass movement occurring when a rockslide transforms into a debris flow. This type of mass movement may cause catastrophic damages because of its high speed and long run-out distance. To achieve a better understanding toward the run-out behavior of this type of landslide, a recent rockslide-debris flow occurred in Verghereto (Northern Apennines of Italy) is studied through field investigation and numerical simulation. The run-out process of this landslide is simulated by an improved depth-averaged model, paying special attention to analyzing the influence of slope gradient and gully channel. The results show that the depth-averaged model can correctly simulate the entrainment and deposition characteristic of this landslide by adopting different basal friction strengths for rockslide region and debris flow region. Entrainment occurs in both high and low slope gradient zones. However, entrainment can only be observed in the high slope gradient zones, while in the low gradient zones the post-failure topography shows accumulation and deposition. The simulation results also demonstrate that the presence of a gully channel is a key factor in determining landslide mobility and run-out distance. In comparison to a landslide with similar size and geological settings but without a gully channel, the run-out distance is much less and the landslide does not develop into a flow.

Keywords: Rockslide-debris flow, Numerical simulation, Solid-fluid transformation, Run-out analysis, Bed entrainment

1. Introduction

A rockslide may transform into a debris flow when it disintegrates and propagates along a confined channel, and this hybrid mass movement is named as rockslide-debris flow. The term “debris flow” indicates partially or fully saturated flow-like movement propagating in gully channel (Hungr et al. 2014) and is distinguished from “rock avalanche” which describes the flow-like movement of essentially dry debris on unconfined slope. A rockslide-debris flow is typically characterized by the presence of a gully channel on the run-out path and it is renowned for the solid-fluid transformation (SFT) occurring during the run-out process. The SFT contributes to the high mobility of these types of landslides. Several factors, such as the disintegration of rock mass (Bowman et al. 2012, Crosta et al. 2007, Davies and McSaveney 2009), entrainment (Aaron and McDougall 2019, Dufresne and Geertsema 2020, Hungr and Evans 2004), and excess pore pressure (Collins and Reid 2019, Sassa and Wang 2005, Wang et al. 2002), have been identified as the possible reasons for the SFT, but the mechanism is still largely elusive because of the complexity of the geo-materials.

Numerous rockslide-debris flows have been reported around the world. Some typical events, such as the Ponti Peak landslide in India (Shugar et al. 2021), the Dujiangyan landslide (Yin et al. 2016) and Jiweishan landslide in China (Xu et al. 2010), and the Mount Meager landslide in Canada (Guthrie et al. 2012), have caused serious economic losses or death tolls to the local communities. Rockslide-debris flows tend to have catastrophic consequences because they are commonly characterized by extremely high speed (a few to tens of meters per second) and long run-out distance (several to tens of kilometers). These catastrophic events remind us the significance of making accurate risk assessment for the potential rockslide-debris flows, and this goal can be achieved only if we have a correct understanding of and can make accurate predictions for the run-out process of these landslides.

Numerical simulation is an efficient tool for the run-out analysis and prediction of rockslide-debris flow, and a variety of physically-based models have been adopted to simulate the run-out process of real landslide events. The models generally in use belong to three categories: 1) depth-averaged

models based on the finite difference method (FDM) (O'Brien et al. 1993, Ouyang et al. 2013, Sassa et al. 2010, Shen et al. 2019, Shen et al. 2018), finite volume method (FVM) (Christen et al. 2010, Mangeney et al. 2003, Xia and Liang 2018), or smoothed particle hydrodynamics (SPH) (Hungr and McDougall 2009, Pastor et al. 2009); 2) discrete models originated from the discrete element method (DEM) (Gao et al. 2021, Wu et al. 2018); and 3) three-dimensional models formulated according to the SPH (Dai et al. 2017, Ghaïtanellis et al. 2021), particle finite element method (PFEM) (Zhang et al. 2015, Zhang et al. 2020) or material point method (MPM) (Li et al. 2021, Soga et al. 2016, Xu et al. 2018). Among these models, the depth-averaged models are probably the most sophisticated and frequently-used in the run-out analysis of real rockslide-debris flow events, mainly because they are more time efficient. Specifically, the depth-averaged model can easily consider entrainment (Cuomo et al. 2016, Iverson and Ouyang 2015, McDougall and Hungr 2005) which is an important phenomenon in rockslide-debris flow modeling. The main difficulty in modeling rockslide-debris flow is how to account for the SFT process. As mentioned above, the mechanism of SFT is still quite elusive, so nearly no existing models can reflect the real physical process of this phenomenon as far as we concerned. However, ignoring the influence of SFT may lead to a wrong prediction of landslide mobility. A simple approach has been adopted in some depth-averaged models to account for the influence of SFT by adopting different rheological models for rockslide and debris flow (Gao et al. 2017, McDougall et al. 2006), and this strategy performed well in improving the simulation results. Due to the above reasons, the depth-averaged models should be more suitable choices for the run-out analysis of the rockslide-debris flow in this study.

Although many studies have analyzed the run-out processes of real rockslide-debris flow events around the world (Gao, et al. 2017, Liang et al. 2020, McDougall, et al. 2006, Xing et al. 2014), few of them have investigated the influence of the geomorphological factors such as slope gradient and gully channel. Moreover, most of these studies did not provide in-depth analysis on the performance of the models according to field measurements of entrainment and deposition.

In this paper we investigate a rockslide-debris flow event recently occurred in the Northern Apennines of Italy (the Verghereto landslide). The landslide was surveyed soon after the failure and

a detailed map of entrainment and deposition was obtained from drone surveys. These data allow validating an improved depth-average model capable of reproducing the complex behavior of the landslide. The model considers entrainment and the influence of SFT is taken into account by changing the basal frictional strength. The influences of slope gradient and the presence of a gully channel on the run-out behavior are discussed, and some insightful conclusions are obtained.

2. The Verghereto landslide

2.1 Geological settings

The Verghereto landslide is located in the Northern Apennines of Italy, approximately 40 km to the south of Cesena City. The area is characterized by steep slopes and deeply incised valleys carved by rivers, with altitudes ranging from 600 m to 900 m above the sea level (Fig. 1).

The bedrock consists of deep marine flysch deposits belonging to the Marnoso-Arenacea Formation. The Marnoso-Arenacea Formation is a turbidite succession representing the filling of the Miocene Apennine foredeep complex, which deposited between the Langhian and the Tortonian (Ricci Lucchi and Valmori 1980). It consists of alternating sandstones and marls layers in variable proportion (Fig. 2a). In the study area, the ratio between coarse and fine strata is about 1/3 and the average bed thickness varies from 0.5 m to 2 m. Both sandstones and marls are strong rocks characterized by high resistance to compression (the uniaxial compressive strength of intact rock specimens typically ranges from 40 MPa to 60 MPa) and high resistance to weathering. When the bedding planes are horizontal or dip into the slope, the high strength of the rock mass ensures the stability of the slopes and supports subvertical cliffs (Fig. 2b). Instead, large failures may occur when the strata dip out of the slope. In this case the rock mass can slide along one controlling bedding plane generating massive rockslides as in the study area.

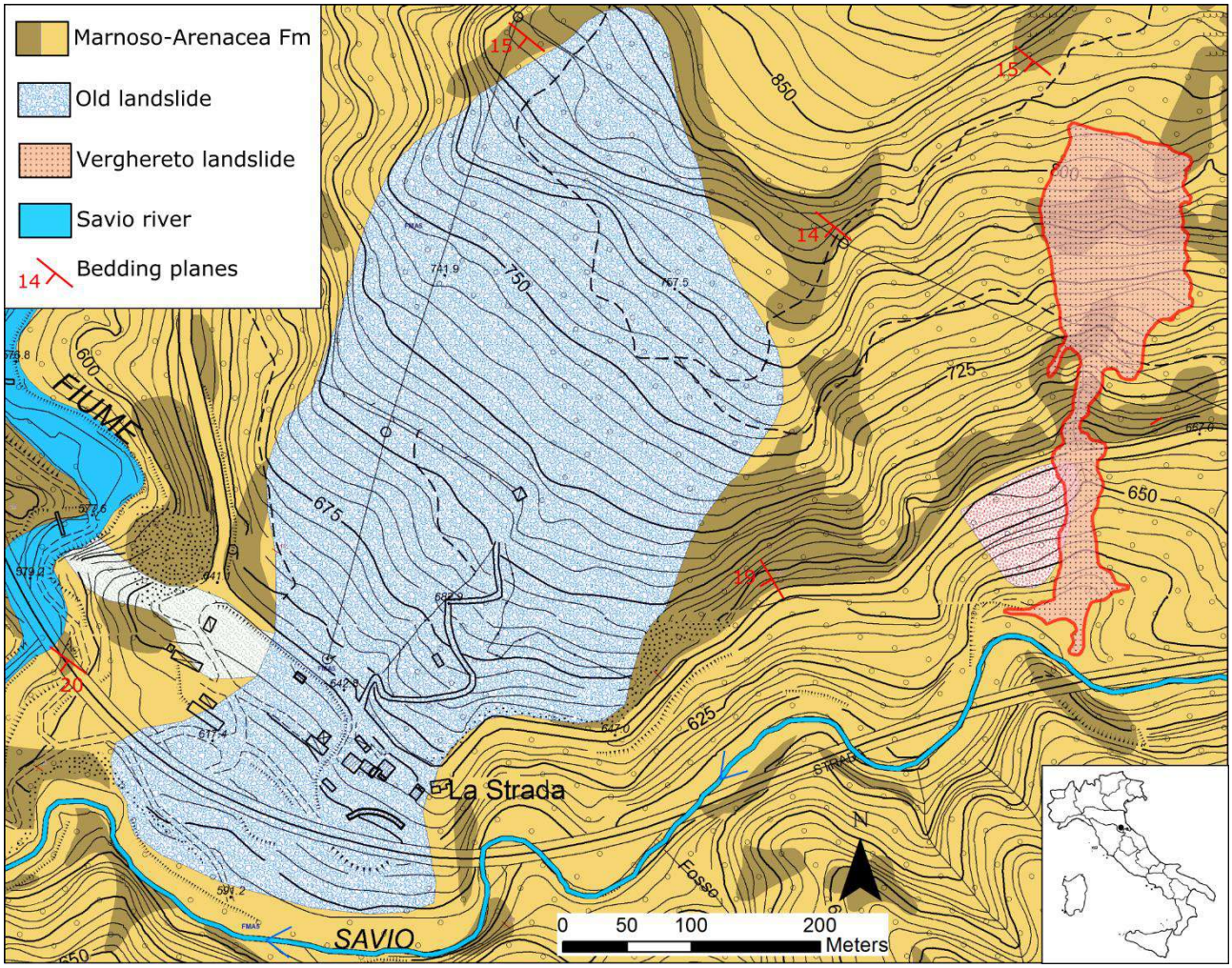

Fig. 1 Geological map of the study area and the locations of the Verghereto rockslide-debris flow and a giant old rockslide-avalanche adjacent to this landslide

Rockslides are the predominant form of instability in the area and are very common on cataclinal slopes where bedding dip is less than slope angle. These failures can occur on bed gradients less than 10°, which is approximately equal to half of the fully-softened angle of shearing resistance of the marls (Berti et al. 1994, Berti et al. 1996). In most cases the failed mass moves as a nearly intact block for a few tens of meters, retaining the original appearance and succession. Less commonly, the failed mass collapses generating dangerous flow-like landslide. In the study area both cases are present. The large landslide shown in the map of Fig. 1 is an old rockslide that did not turn into a flow, as suggested by the rectangular shape of the deposit and by lack of a transportation channel. Instead, the Verghereto landslide (in red) mobilized into a flow that advanced down a gully to the foot of the slope.

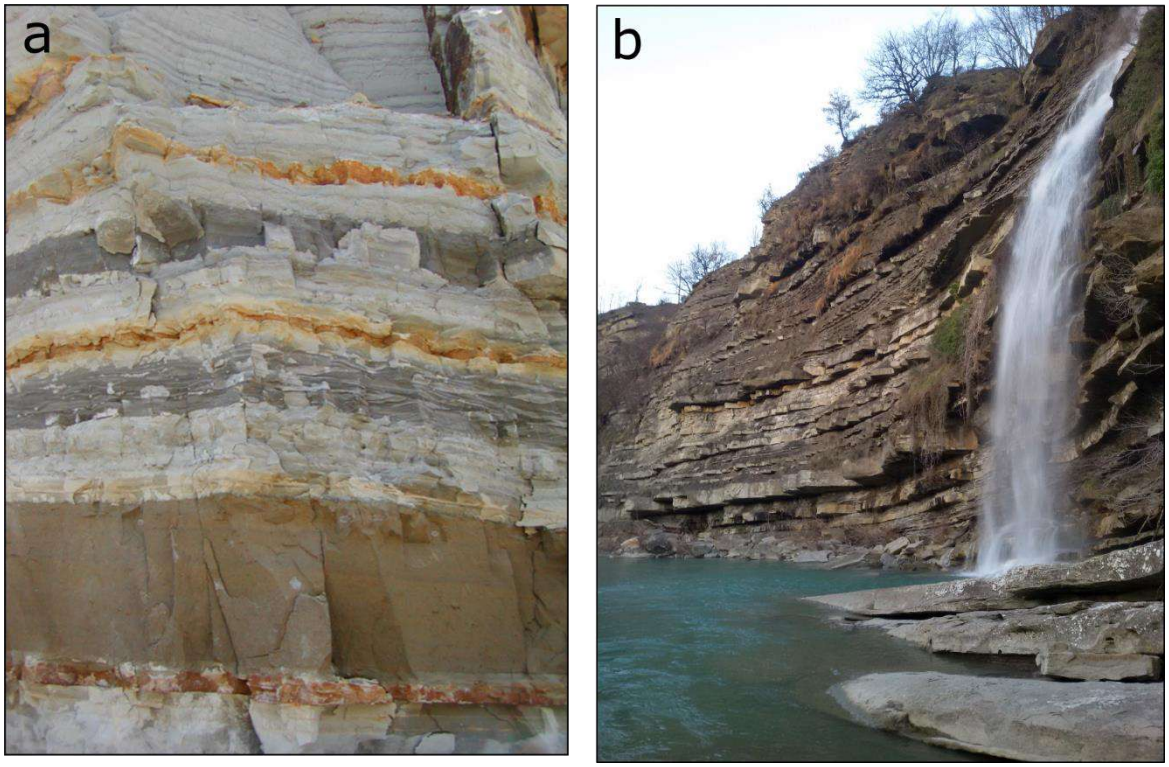

Fig. 2 Alternating sandstone and marls layers which consist of the sliding mass of the Verghereto rockslide-debris flow

2.2 The landslide

The Verghereto landslide occurred around 5:00 a.m. in the morning of May 13, 2019. A rock mass with a volume of nearly 40,000 m^3 detached from the upper part of the slope sliding along a gently dipping bedding plane. The toe of the failed mass came out the slope, disintegrated into rock debris, and transformed into a debris flow that traveled downslope for about 300 m reaching the main river (Fig. 3a). The landslide destroyed a local road, 2.4 hectares of forest, and threatened the pylons of the highway that passes on the valley floor partially closing the River Savio. The landslide was triggered by a high-intensity short-duration rainfall that caused severe flooding and other landslides in the area. The failure was preceded by a rainfall of about 80 mm in 15 hours, with a peak intensity of 8 mm/h and a return period of 10-15 years (Fig.New1).

The map in Fig. 4 shows the three geomorphological zones that were identified in the field soon

after the event. Zone A is the source area of the landslide. It consisted of a rockslide that moved essentially as a rigid block. Apparently, the slide did not acquire enough momentum to carry all the rock mass beyond the foot of the slope, and about one third of the mass stopped at 30-40 m from the detachment scarp. Sliding took place at a depth of about 10 m below the ground surface, at the top of a marlstone layer dipping 15° to southwest (Fig. 3b). The rock exposed on the sliding surface was fresh and stiff and we did not notice any appreciable difference with the other marls layers outcropping on the trench walls. The lack of previous landslides indicated that the slide was a first-time failure.

The front part of the rockslide collapsed and dropped about 28,000 m^3 of fragmented rock to the slope below (zone B in Fig. 4; Fig. 3d). Just below the source area, the slope is very steep (over 35° degrees). Here the landslide stripped the vegetation and the soil cover over an area of about 4500 m^2, leaving evident scratches on the rock surface. Further downhill the slope angle decreases to less than 30° allowing some crushed rocks and coarse debris to accumulate loosely in the lower part of the zone.

Part of the landslide material then entered a small, ephemeral gully incised in colluvium and mobilized into a debris flow (zone C in Fig. 4). Along the steep reach of the gully the debris flow showed significant bulking by scouring and erosion and created a channel 15 m wide and 2-3 m deep (Fig. 3c). As the gradient decreased to 20°-25°, the flow started to deposit within the channel and came to rest at the foot of the slope. In the accumulation lobe the debris was on average 1-3 m thick with an overall volume of approximately 15,000-20,000 m^3. The presence of scouring, lateral levees, and trees damaged or debarked by the impact with debris indicate that the flow was extremely rapid.

One week after the failure we conducted a drone survey of the landslide. Five flights were done using a DJI Spark UAV to cover an area of about 30.000 m^2. DJI Spark is a mini-drone equipped with GPS/GLONASS positioning system and a 12 MP CMOS camera. Images were taken from a flight elevation of about 30 m retaining an overlap of 80% along the flight path. Nine ground

controls points were surveyed with a differential GPS receiver at the time of the flight. The post-failure topographic model was obtained with the Structure-from-Motion photogrammetric technique. Vegetated areas were masked out in the analysis in order to extract the digital terrain model of the bare ground. The final model has a resolution of 5 cm/pixel and a total RMS error of 0.2 m. Post-failure topography was compared with the pre-failure digital terrain model (DTM) available for the area with a 5 m resolution and a maximum error of 1.2 m. Estimates of change in vertical elevation were finally computed by subtracting ground elevation of the two DTMs (Difference of DTMs, DoD; Fig. New2). Errors from individual DTMs propagate into the DoD resulting in a minimum level of change detection of about 1.5 m (rounded square root of the sum of squares of individual errors).

The DoD (Fig. New2) cleary show the deep trench behind the rockslide body and the displaced rock block in zone A. The translational movement of the rockslide created negative topography in the trench and positive topography in the deposit. Zone B is characterized by a slight positive topography generated by the debris accumulated on the scratched ground surface. Zone C shows a complex alternation of erosion and deposition caused by the debris flow. In these zones, however, elevation changes are difficult to interpret because of the low accuracy of pre-failure topographic data.

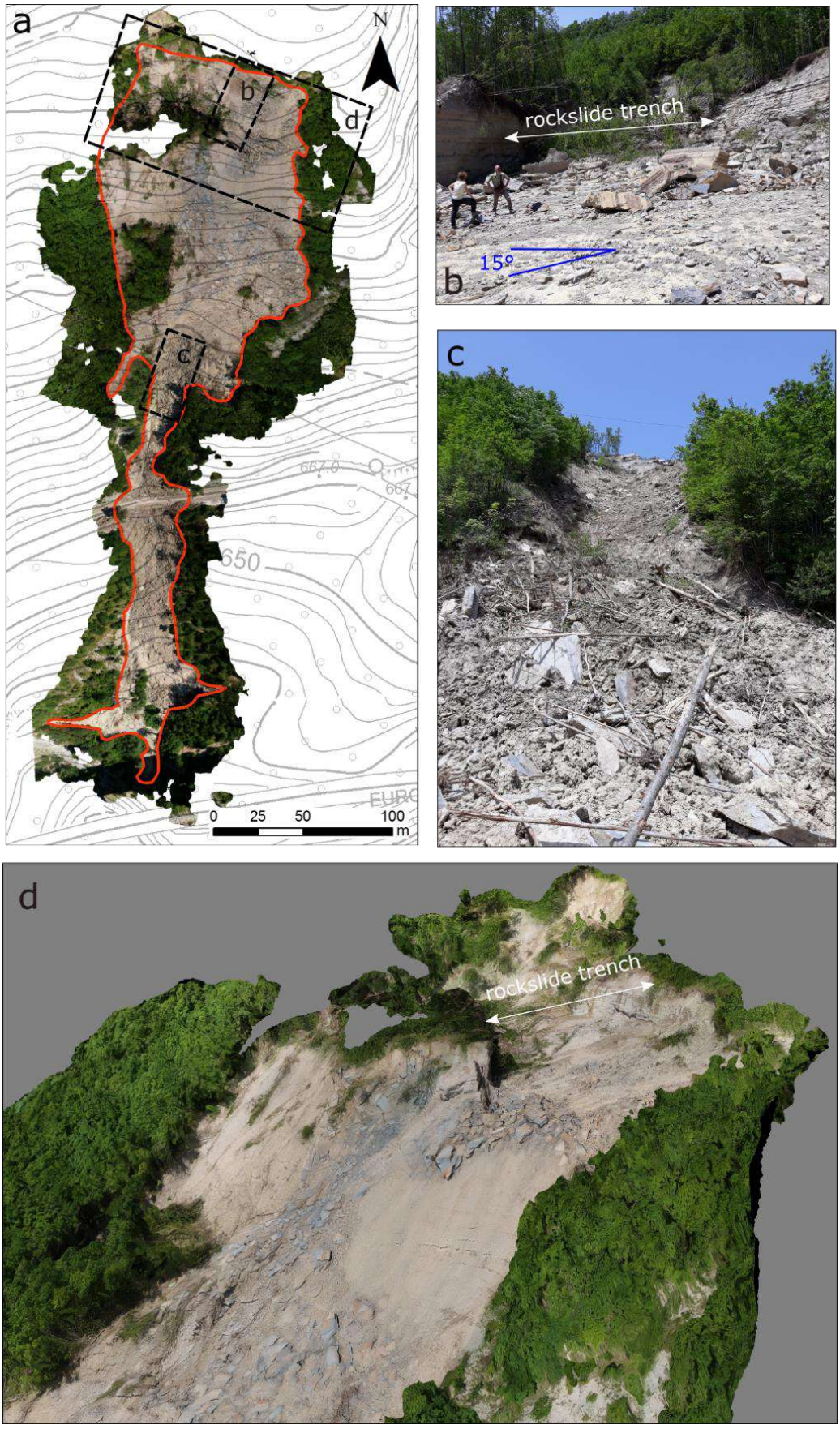

Fig. 3 a) Top view of the rockslide, b) the trench exposed in the source zone after the occurrence of the rockslide, c) debris deposit in the channel, and d) the steep slope below the source zone

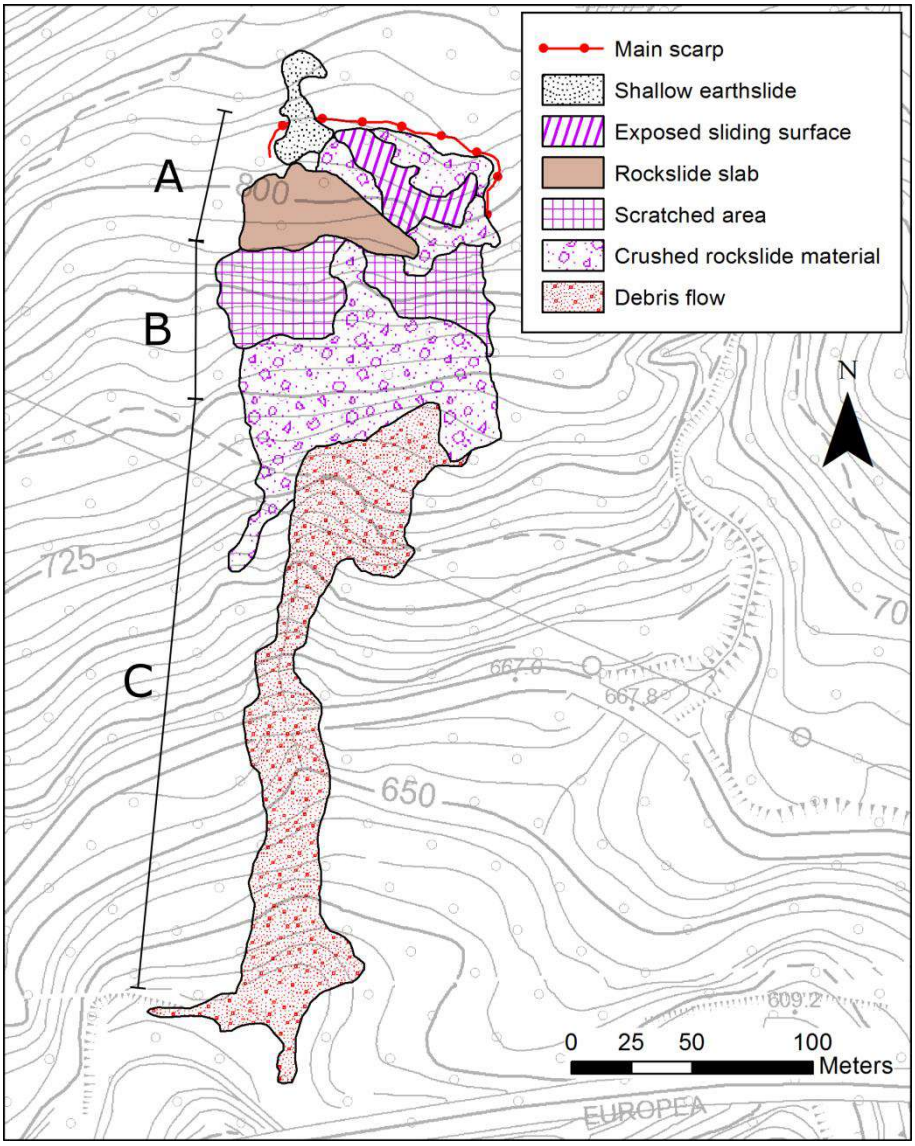

Fig. 4 Characteristics of the deposit in different regions of the landslide influenced zone and the three geomorphological zones identified after the event. A is the source area of the landslide, B is the transformation zone, and C is the debris flow zone

3. Methodology

3.1 Numerical model

An improved finite difference model (Shen, et al. 2018) is adopted to simulate the run-out process of the Verghereto landslide. This model is built in a global Cartesian coordinate, with the positive

direction of z axis parallel to the opposite direction of gravity. Similar to the typical depth-averaged models, this model consists of one mass balance equation and two momentum balance equations, which are given by:

$$\frac{\partial h}{\partial t}+\frac{\partial Q_x}{\partial x}+\frac{\partial Q_y}{\partial y}=-\frac{\partial Z}{\partial t}=\frac{\tau_b-\tau_e}{\rho_e\sqrt{v_x{}^2+v_y{}^2}} \tag{1}$$

$$\frac{\partial Q_x}{\partial t}+\frac{\partial Q_x{}^2/h}{\partial x}+\frac{\partial Q_xQ_y/h}{\partial y}=-\frac{\partial k_x gh^2/2}{\partial x}+\frac{(Ag+B)h\tan\alpha}{\tan^2\alpha+\tan^2\beta+1}-\frac{\tau_b A_b h v_x}{m\sqrt{v_x{}^2+v_y{}^2+v_z{}^2}} \tag{2}$$

$$\frac{\partial Q_y}{\partial t}+\frac{\partial Q_xQ_y/h}{\partial x}+\frac{\partial Q_y{}^2/h}{\partial y}=-\frac{\partial k_y gh^2/2}{\partial y}+\frac{(Ag+B)h\tan\beta}{\tan^2\alpha+\tan^2\beta+1}-\frac{\tau_b A_b h v_y}{m\sqrt{v_x{}^2+v_y{}^2+v_z{}^2}} \tag{3}$$

where: h is flow depth; $Q_x = v_x h$ and $Q_y = v_y h$ are mass fluxes in x and y directions; v_x, v_y and v_z are depth-averaged velocities in x, y and z directions; k_x and k_y are lateral pressure coefficients in x and y directions determined according to soil state (Ouyang et al. 2015); g is gravitational acceleration; A and B are terms related to static and centrifugal/centripetal normal forces on bed; α and β are dip angles in x and y directions; τ_b is the basal shear stress of flow; τ_e is the shear stress in erodible mass; ρ_e is the bulk density of entrained mass; A_b is the bottom area of a control volume; m is the mass of flow in the control volume. The expressions of A, B, A_b, τ_b and τ_e are given by:

$$A=1+\frac{\partial k_x h^2/2}{\partial x}\tan\alpha+\frac{\partial k_y h^2/2}{\partial y}\tan\beta \tag{4}$$

$$B=\frac{C_x}{\cos\alpha}\left(\frac{v_x}{\cos\alpha}\right)^2+\frac{C_y}{\cos\beta}\left(\frac{v_y}{\cos\beta}\right)^2 \tag{5}$$

$$A_b=\Delta x\Delta y\sqrt{\tan^2\alpha+\tan^2\beta+1} \tag{6}$$

$$\tau_b=\sigma(1-r_{ub})\tan\varphi_b'+c_b' \tag{7}$$

$$\tau_e=\sigma(1-r_{ue})\tan\varphi_e'+c_e' \tag{8}$$

in which: C_x and C_y are bed curvatures in x and y directions; Δx, Δy are the sizes of a control volume in x and y directions; σ is the normal stress on bed; r_{ub} and r_{ue} are the pore pressure coefficients (the ratio of the pore pressure to the total normal stress) in flow bottom and erodible mass; φ' and c' are effective frictional angle and cohesion. The subscripts b and e refer to flow bottom and erodible mass, respectively.

244

245 A finite difference scheme is utilized to solve the above governing equations, and the details of the
246 numerical scheme could be found in Shen, et al. (2018).

247

248 ## 3.2 Simulation setup

249

250 . Within the area we selected a region which covers the whole run-out zone of the landslide as the
251 computational domain. The size of this domain is 522 m in x direction (N-S) and 291 m in y
252 direction (E-W). Uniform computational grids 3 m long in both x and y directions are adopted in the
253 present study, and the maximum time step is 0.02 s.

254

255 According to the landslide characteristic described in Section 2, we divided the computational
256 domain into two regions (Fig. 5). The first region is the area above the gully head ($x < 270$ m),
257 which include the source zone of the rockslide and the steep slope below (zones A and B in Fig. 3).
258 The second region is the zone below the gully head, where the rockslide turned into a debris flow
259 (zone C in Fig. 3). According to our field observations, the landslide essentially moved like a solid
260 in the first region and like a flow in the gully.

261

262 Although the transformation of rockslide and debris flow is gradual rather than sudden, in order to
263 simulate the complex behavior of the Verghereto landslide with a single-phase model, we must
264 necessarily assume different material properties in the two regions. A simple way to do it is to
265 assign a high frictional strength in region 1 (where the landslide moved like a slide) and a low
266 frictional strength in region 2 (where the landslide moved like a flow). Different values of the
267 frictional strength were obtained by adopting different values of the pore pressure coefficient r_u in
268 the two regions. In particular, we used a pore pressure coefficient of zero to simulate the high
269 frictional strength at the base of the landslide, and a pore pressure coefficient of 0.3 to simulate low
270 frictional strength.

271

272 This assumption is basically reasonable, since the basal pore pressure is usually higher when a

landslide is in fluid state than in solid state. All the other model parameters (density, friction and cohesion) were assumed to be identical in the whole domain.

Based on these assumptions, three groups of simulation were conducted using the parameters listed in Table 1. According to field investigation, the thickness of erodible soil cover was set to be 1.5 m in the whole region except in the source zone of the rockslide where the bedrock outcrops. The erodible mass is required to have a higher pore pressure than the sliding mass in order to be entrained. Here, erodible mass is assumed to have the same effective strength parameters (c' and φ') as the sliding mass, while its pore pressure coefficient r_{ue} takes a higher value (r_u=0.8).

Table 1 Parameters for simulating the Verghereto landslide

Group	**Pore pressure coefficient in R1** r_{u1}	**Pore pressure coefficient in R2** r_{u2}	**Basal effective cohesion** c' (kPa)	**Basal effective friction angle** φ'
S1	0.0	0.0	5	30
S2	0.3	0.3	5	30
S3	0.0	0.3	5	30

Notes: R1 and R2 refer to Region 1 and Region 2, respectively.

4. Results

4.1 Depositional characteristics

In Fig. 5, we illustrate the difference between the pre-failure and post-failure topography obtained from simulations (a-b-c) and measurements (d). The analysis S1 simulates a landslide with high frictional resistance at the base (r_u=0 in the whole domain). In this scenario, the landslide stops in the upper part of the slope and reaches a much smaller run-out distance than that observed in the field. However, the computed depositional pattern agrees well with the survey data in Zone A and B (comparing simulation results with Fig. 4 and Fig.3d). As mentioned above, in region 1 the

landslide caused erosion on steep slopes and deposition on gentle slopes. The model captures this spatial variability, showing entrainment on the steep slopes right below the source zone (negative DEM difference ranges from -1.0 m to -1.5 m) and deposition on the gentle slopes further downhill (positive DEM difference ranges from 4.0 m to 5.0 m).

By assuming low frictional strength in the whole domain (r_u=0.3; simulation S2) the model predicts a larger mobility of the landslide (Fig. 5b). In this case, the landslide spreads over a much broader region than the measured one, leading to a significantly inaccurate prediction of the run-out. In particular, the landslide runs downslope laterally rather than flowing into the gully (Fig. 5b). These results indicate that in region 1 the frictional strength at the base of the landslide should be relatively high, so that most of the fragmented material can come to rest in this area.

This is confirmed by the results of simulation S3, which provides the best agreement with reality. By adopting a high friction in region 1 and a low friction in region 2 simultaneously, part of the material stops below the source area and part continues downslope as a flow. With this combination of r_u the model can simulate the debris flow (zone C in Fig. 4) and the landslide reaches a run-out distance similar to the measured one (Fig. 5d). Moreover, the model correctly predicts erosion in the upper reach of the channel and deposition in the lower reach, where the slope becomes gentle (Fig. 5c). The above analysis indicates that friction change caused by the SFT plays a significant role in the run-out behavior of this landslide. And we may not be able to correctly simulate the run-out process if the SFT is neglected. Additionally, although the single-phase model cannot actually depict the complicated physical process of the SFT, the above simple method could improve the simulation results of those landslides involving such a complex SFT phenomenon by adopting frictional strengths for the sliding mass under the two different states (solid and fluid states).

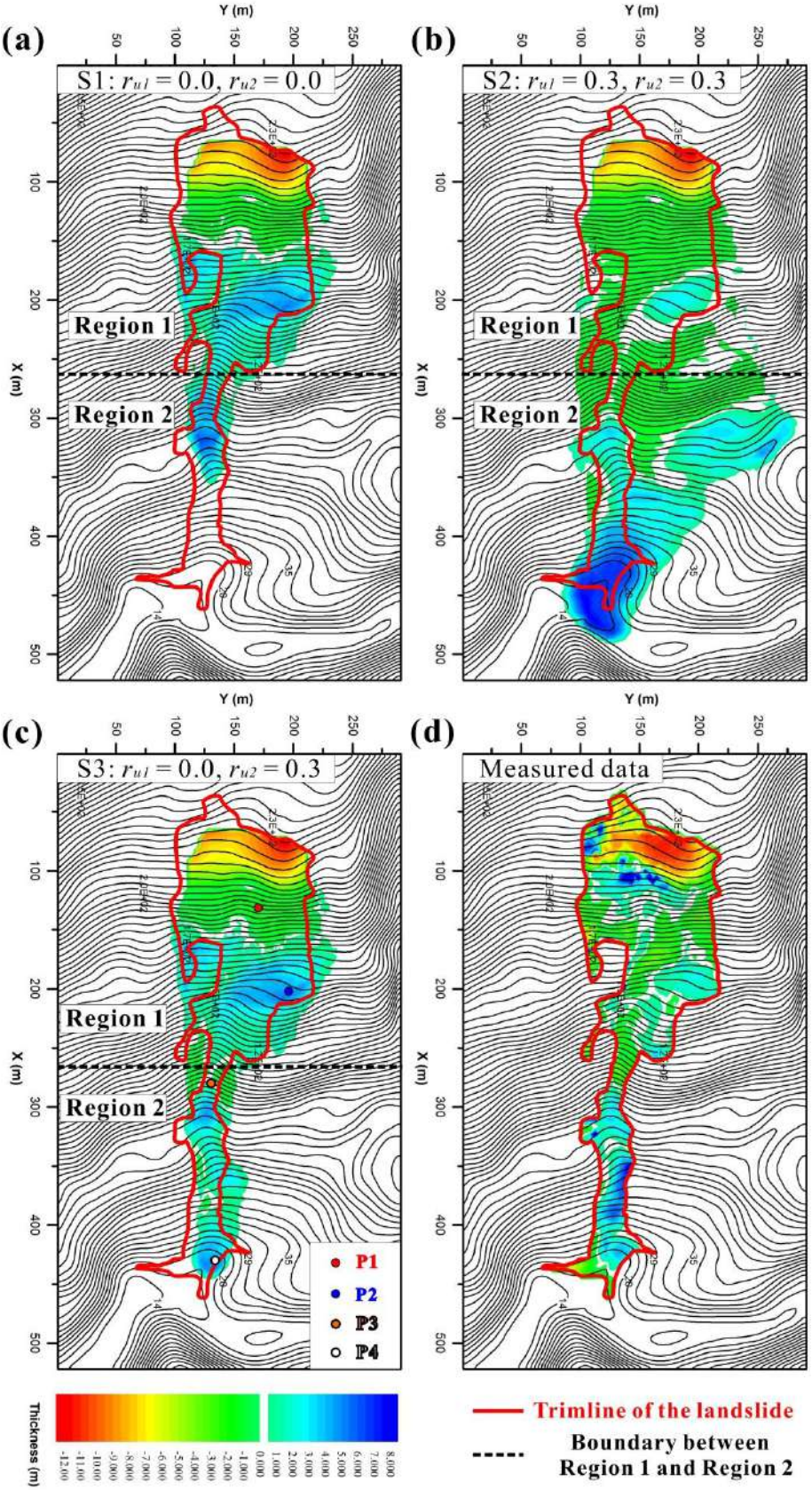

Fig. 5 Digital elevation differences between pre-failure and post-failure topographies in the landslide zone obtained from simulations and field survey

4.2 Velocity and entrainment

The total average velocity and entrainment time curves of the landslide in the three simulations (S1-S3) are illustrated in Fig. 6. The four turning points shown on the average velocity curve of simulation S3 (Fig. 6a) indicate the first velocity peak (t_1), the turning point between the first deceleration stage and the second acceleration stage (t_2), the second velocity peak (t_3), and the time when the motion of the landslide basically stops (t_4). From 0 s to t_1, the landslide accelerates rapidly after it detaches from the bedrock and propagates to the steep slope just below the detachment area. Then the landslide reaches a low slope gradient area (lower part of zone B, Fig. 4), resulting in a dramatic drop of the average velocity from t_1 to t_2. The landslide enters the gully head at around t_2. Here the model predicts a second slight acceleration stage (from t_2 to t_3) which should be attributed to both SFT and the steep topography in the downstream part of the gully head. Finally (from t_3 to t_4) the landslide comes to rest gradually. The difference between simulations S1 and S3 is that the second acceleration stage does not exist in S1, since in this case the reduction in frictional strength is not taken into account. Therefore, in S1 the landslide stops quickly after entering the gully showing a small run-out distance. By contrast, in S2 the landslide runs too fast and too distant, and the predicted velocity and entrainment are clearly overestimated.

The total volume curve of simulation S3 (Fig. 6b) indicates that the landslide is likely to have entrained a large amount of loose soil before reaching to the gully head. This extra volume from entrainment may potentially generate the source material for the mass flow in the gully. The volume of the landslide probably doubled (from approximately 28,000 m^3 to around 56,000 m^3) through entrainment.

The thickness and entrainment distributions of the landslide (in group S3) at the above four moments (t_1-t_4) are presented in Fig. 7. The thickness distributions at the four moments support our above analysis toward the velocity change process of the landslide. By contrast, the entrainment distribution characteristic of the landslide is relatively simple (Fig. 7), indicating the landslide may

entrain almost all the superficial loose mass on the slope wherever the landslide runs over.

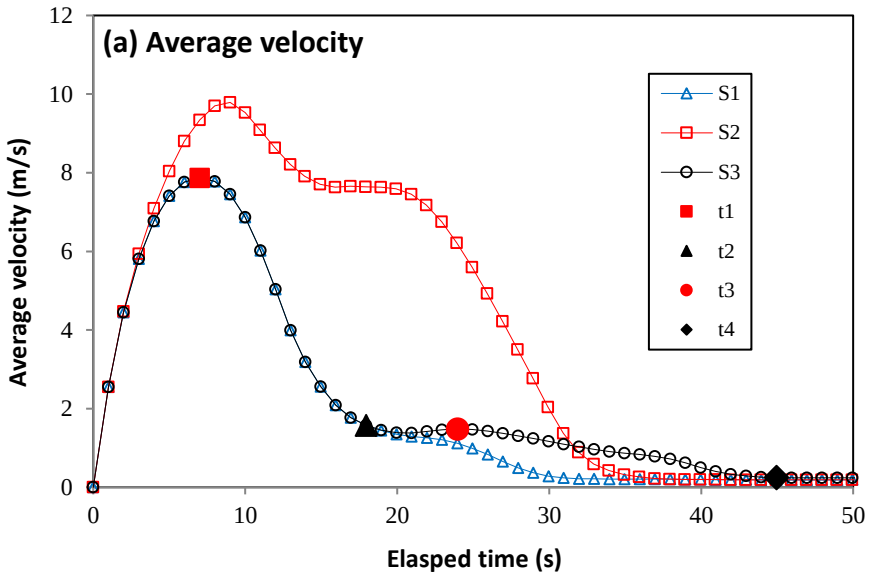

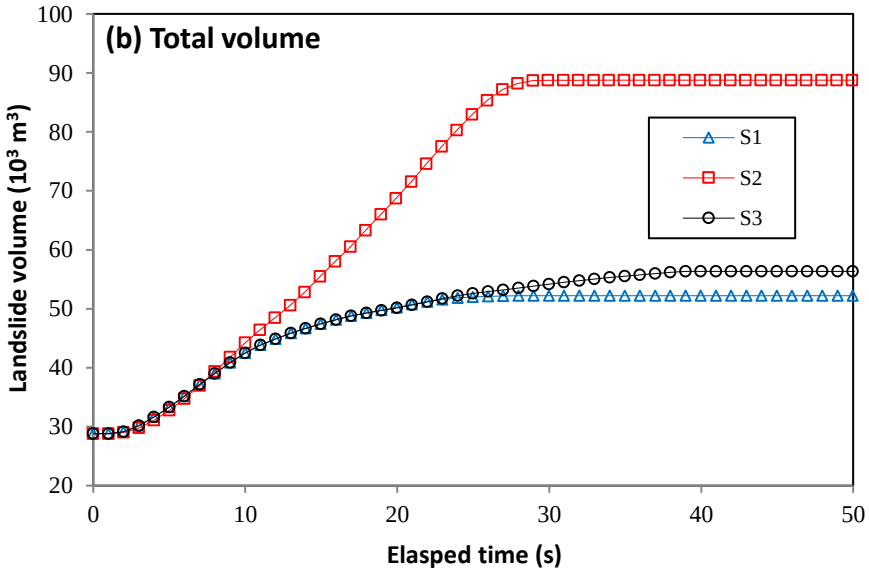

Fig.6 Simulated time curves of the (a) average velocity and (b) total volume of the Verghereto landslide

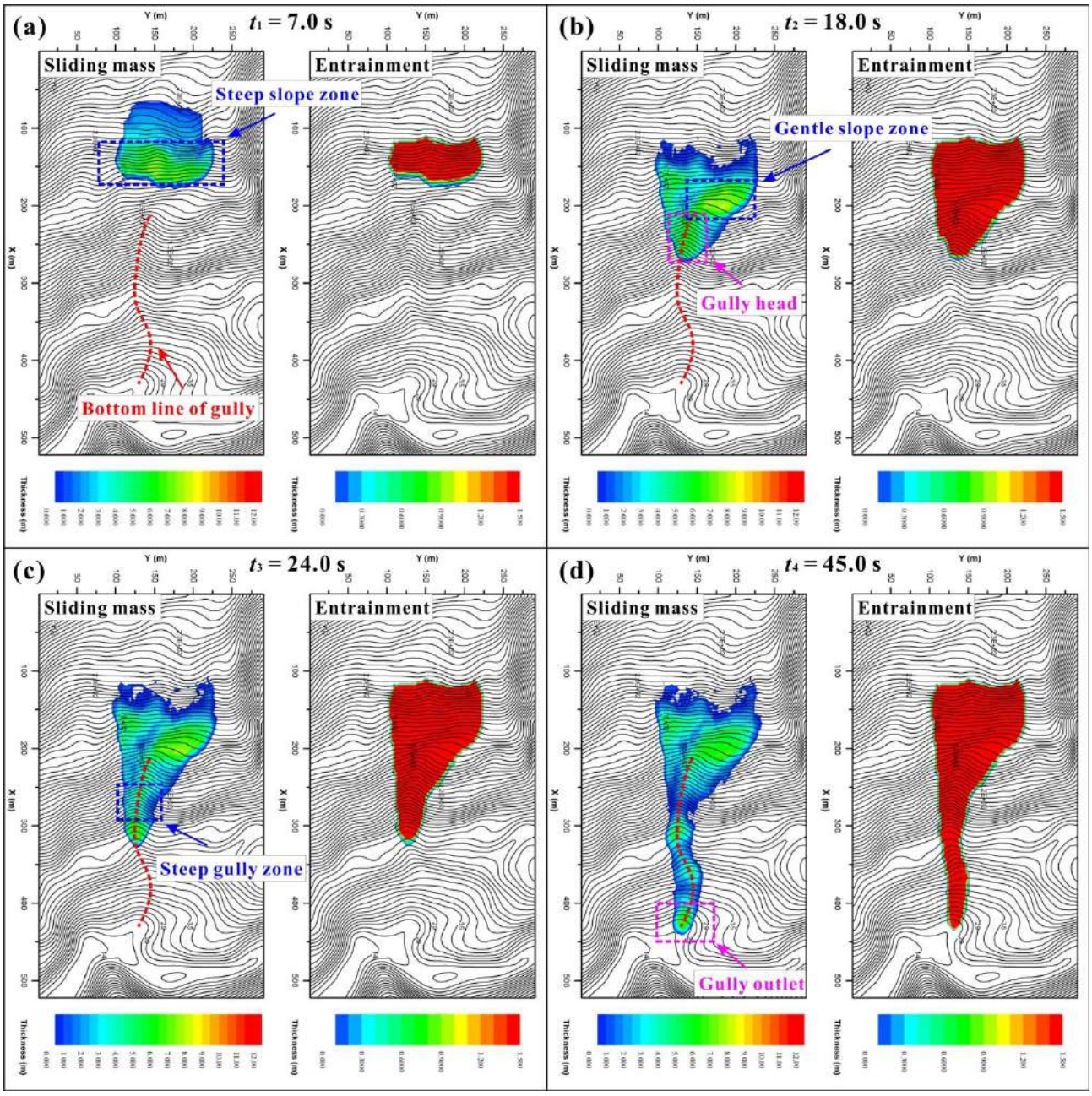

Fig. 7 Thickness and entrainment distributions of the landslide at four moments in S3. t_1 corresponds to the time when the landslide has the highest kinetic energy, t_2 is the time when part of the landslide starts to enter the gully head, t_3 is the time when the landslide reaches the second velocity peak, and t_4 corresponds to the time when the landslide basically comes to rest.

4.3 Influence of topography

Four numerical gauge points (P1-P4) in the landslide area are selected to analyze the influence of topography (slope gradient and gully channel) on the simulated dynamic characteristics (thickness,

367 velocity and Froude number) of the landslide at four different locations, and the simulation results
368 of group S3 is used to conduct this analysis. The locations of these gauge points are shown in Fig.
369 5c. P1 and P2 are located in region 1 where the landslide is in 'solid state', while P3 and P4 are
370 points located in region 2 where the landslide has transformed into a debris flow. P1 and P3 are
371 approximately in the middle part of the steep slope gradient zones in region 1 and region 2 (in
372 gully), respectively. For comparison, P2 and P4 are selected from the low slope gradient zones in
373 region 1 and region 2, respectively. The flow thickness h and depth-averaged velocity v are directly
374 available from the simulation results, while the Froude (Fr) number is calculated using $\mathrm{Fr} = v/\sqrt{gh}$.
375 Fr number is a dimensionless variable reflecting the relationship between flow inertia and gravity.
376 At P1 and P3 where the slopes are steep, the thickness of the landslide (Fig. 8a) increases fast when
377 the front of the landslide arrives, and then decreases gradually to less than 1 m. The final DEM
378 differences (net change in elevation) in these zones are less than zero, so the deposit there has an
379 appearance of entrainment. However, at P2 and P4 the sliding mass accumulates and finally stops
380 propagating, demonstrating an opposite appearance of deposition. Actually, entrainment should
381 occur in both steep and gentle slope gradient regions, but the apparent entrainment is only revealed
382 in steep slope zones. The thickness of the landslide at P3 remains at a relatively stable and thin level
383 (about 1.5 m) which lasts for around 15 s after the arrival of landslide front, while at P1, the
384 thickness decreases quickly after the arrival of landslide front. These different thickness curves
385 indicate that on the steep slopes in Region 1 (P1) the landslide propagates like a surge wave, while
386 on the steep slopes in Region 2 (P3), the landslide probably behaves like a plug flow due to the
387 confinement of lateral propagation from the gully channel. The velocity curves (Fig. 8b) illustrate
388 that the velocity of landslide is generally higher when it propagates on steep slopes than on gentle
389 slopes (Fig. 8b). And the peak velocity of landslide on steep slopes (around 8.0 to 9.0 m/s) is about
390 twice of the peak value on gentle slopes (approximately 4.0 to 5.0 m/s). The Fr number curves at P2
391 and P4 are similar. At P2 and P4, the Fr number peaks at the arrival of landslide front, and then
392 decreases quickly because the sliding mass accumulates and comes to rest on the gentle slopes. By
393 contrast, the Fr numbers at P1 and P3 show some different tendencies. At P1 and P3, the Fr number
394 peaks when the landslide front arrives, and then the number drops quickly until it rises up again.
395 After reaching at the first valley value, at P1 the Fr number increases rapidly to a second peak larger

than the first one, and then the number slumps to a low value. However, at P3 the Fr number increases only slightly until reaching at a relatively steady value (around 1.5) which lasts approximately 10 s, and then gradually decreases to a low value. These difference tendencies on Fr number between P1 and P3 is probably caused by the presence of the gully channel and its influence on the dynamic process of a landslide. This influence from gully will be discussed in the Discussion section. In summary, the topography on the path has a significant influence on the dynamic characteristic of this landslide. At locations on steep slopes, the landslide passes over quickly and finally shows entrainment. Conversely, at low slope gradients regions, the landslide comes to rest fast and eventually produces deposition. The existence of a gully channel also alters the dynamic characteristic of the landslide.

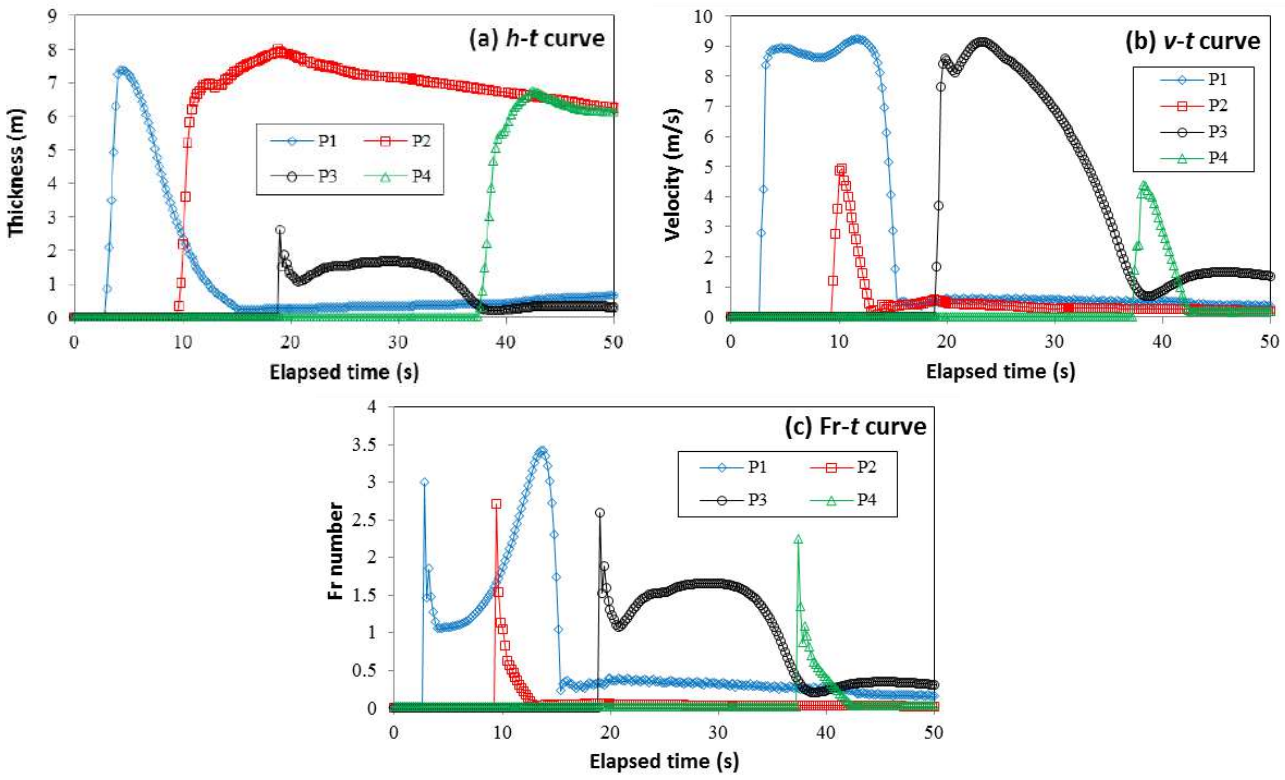

Fig. 8 Time curves of thickness, velocity and Froude (*Fr*) number of sliding mass at four locations P1 to P4. P1 is on the steep slope of Region 1, P2 on the low slope gradient zone in Region 1, P3 on the steep slope at the gully head and P4 on gully outlet.

5. Discussion

As mentioned above, the existence of a gully channel may play an important role in determining the dynamic characteristic of a landslide. In field, we observed an interesting phenomenon that the existence of a gully seems to increase the final run-out distance of a rockslide. In rockslides with similar geological setting, those rockslides have a gully on the slope, similar to the Verghereto landslide in this study, tends to have a larger run-out distance which usually extends to the slope toe, while the rockslides without a gully normally deposit in the middle part of the slope which is far away from the slope toe.

To illustrate the influence from channel, in this section we simulate the Verghereto landslide in the condition of without a channel. Then four imaginary numerical tests (S1-nTnG, S2-nTwG, S3-wTnG and S4-wTwG) are conducted to investigate the generalized scenarios.

The simulation setups of the Verghereto landslide without the presence of a channel are the same as those in S3 expect for the topography. In this simulation, the channel on the slope is artificially removed by adjusting the elevation around the gully. The result is present in Fig. 9, which obviously shows a reduction in the run-out distance due to the absence of a channel.

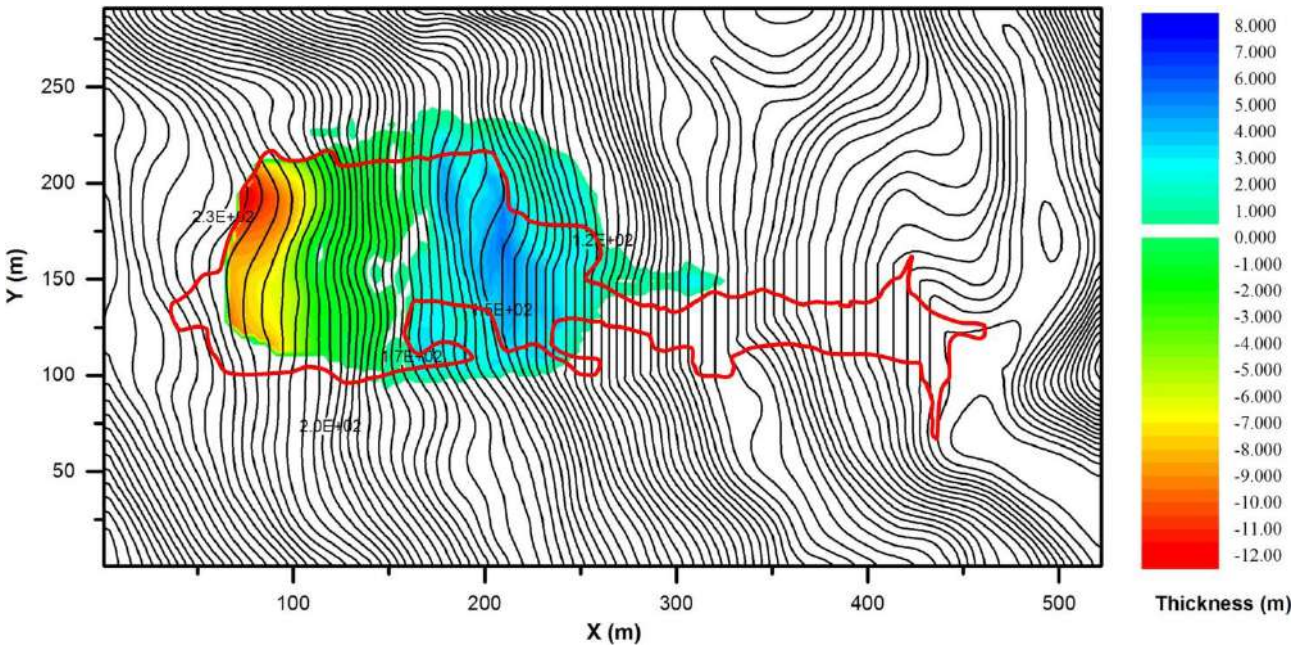

Fig. 9 Simulation result of the Verghereto landslide in the condition without the presence of a channel on the slope

The simulation setups for the other four generalized numerical tests are listed in Table 2. The schematic diagram of these numerical tests is shown in Fig. 10. In these tests, a 10 m thick, 80 m wide and 60 m long rock block is assumed to detach from the bedrock in a rock scarp and forms a rockslide. Then the rockslide propagates on a 25° slope next to the rock scarp. The landslide area is divided into two regions similar to what we have done in the simulation of the Verghereto landslide. The slope above the gully head (x > 200 m) is region 1, while the slope below the gully head is region 2. The pore pressure coefficients in these two regions have different combinations in different groups (Table 2).

Table 2 Parameters for simulating ideal soil collapse experiments

Group	**Existence of A channel**	**Pore pressure Coefficient in R1** r_{u1}	**Pore pressure Coefficient in R2** r_{u2}	**Basal effective cohesion** c' (kPa)	**Basal effective friction angle** φ'
S1-nTnG	No	0.25	0.25	5	30
S2-nTwG	Yes	0.25	0.25	5	30
S4-wTnG	No	0.25	0.40	5	30
S4-wTwG	Yes	0.25	0.40	5	30

Notes: R1 and R2 refer to Region 1 and Region 2, respectively.

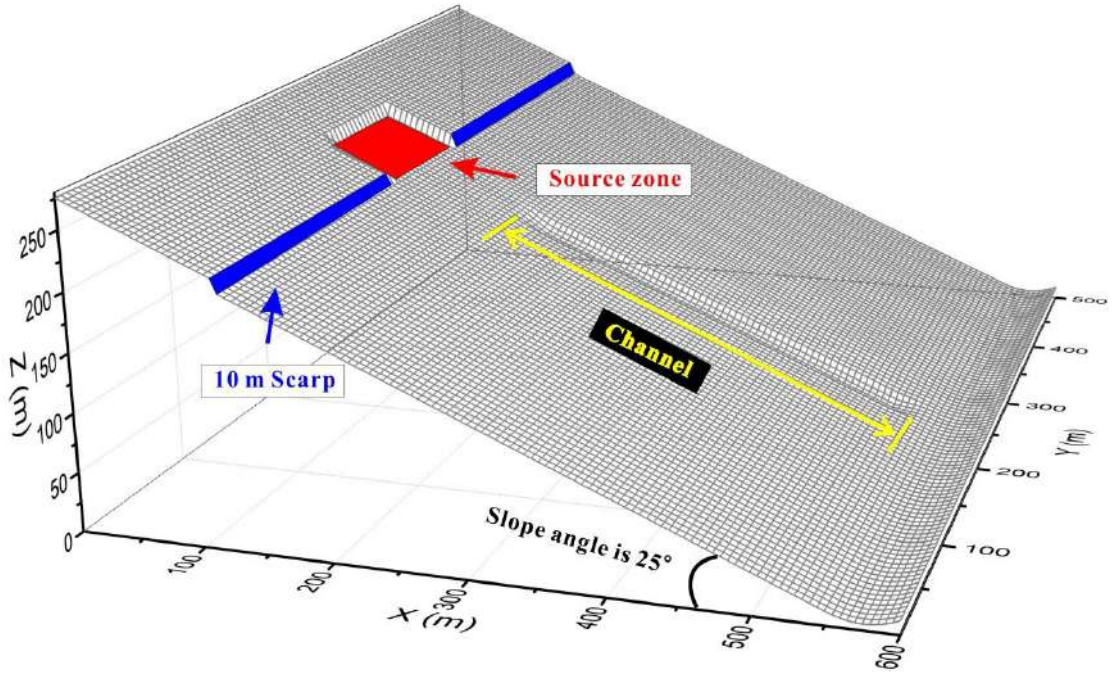

Fig. 10 Schematic diagram of the ideal rock collapse experiment with a channel on the slope

The simulation results illustrate that the existence of a channel can obviously increase the run-out distance (Fig. 11), no matter there is SFT or not. Without SFT and the channel (Fig.11a), the front of final deposit reaches to x = 280 m, while the final landslide front can reach to x = 360 m if there is a channel on the slope (Fig. 11b). Similarly, when there is SFT, the rockslide will has a larger run-out distance than that one without SFT (Fig. 11a), but the movement of the rockslide still will stop on the middle part of the slope while there is no channel on the slope (Fig. 11c). By contrast, the landslide may reach to the slope toe if there is a channel (Fig. 11d). These results indicate that SFT may not be the only factor contributing to the large run-out distance of the landslide. The existence of a gully can also promote the run-out distance. The promotion effect of a gully on the run-out distance of a landslide may simply because the gully constrained the lateral spreading of the landslide. When the landslide propagates on a relatively uniform slope (Fig. 11a and 11c), it propagates forward and laterally simultaneously. The lateral spreading process will consume part of the kinetic energy, so the deposit has a smaller run-out distance but a larger lateral spreading area. Conversely, the channel reduces the lateral spreading and the energy consumption caused by it, so the landslide reaches a larger run-out distance but a much smaller lateral spreading area. This conclusion could be helpful for us to conduct a quick prediction on the risk of potential rockslides

similar to the Verghereto rockslide. Those with a gully channel on the slope may pose higher risk on the infrastructures in the gully outlet (slope toe), while the potential rockslides without a gully on slope mainly endanger the properties in the middle part of the slope. The average velocity curves of these numerical tests agree with the above analysis (Fig. 12). The existence of a channel can reduce the rate of deceleration and produce a larger run-out distance.

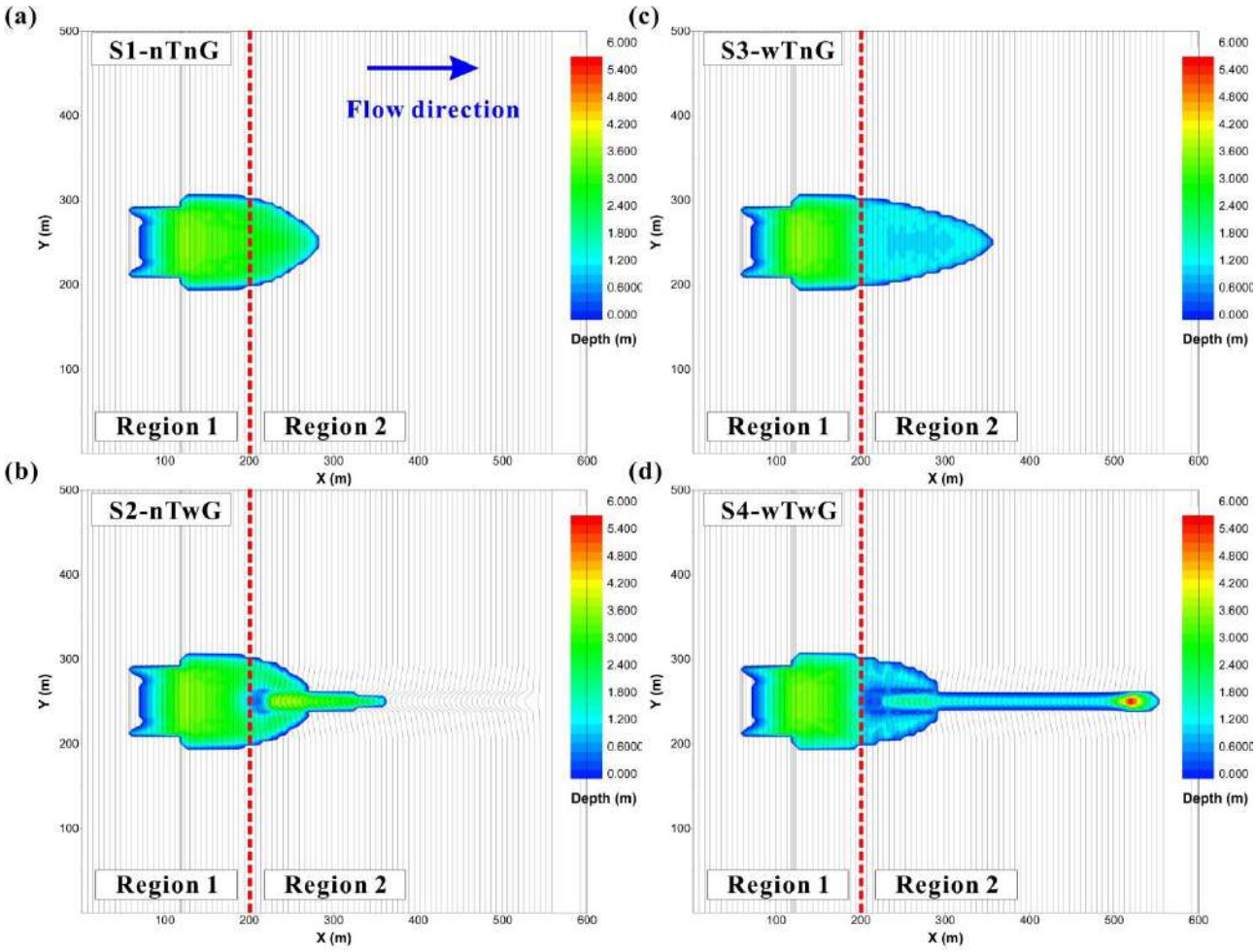

Fig. 10 Simulation results of ideal rockslides on a slope with different parametric and topographic conditions. The four graphs correspond to (a) without both SFT a channel and, (b) without SFT but with a channel, (c) with SFT but without a channel, and (d) with both SFT a channel

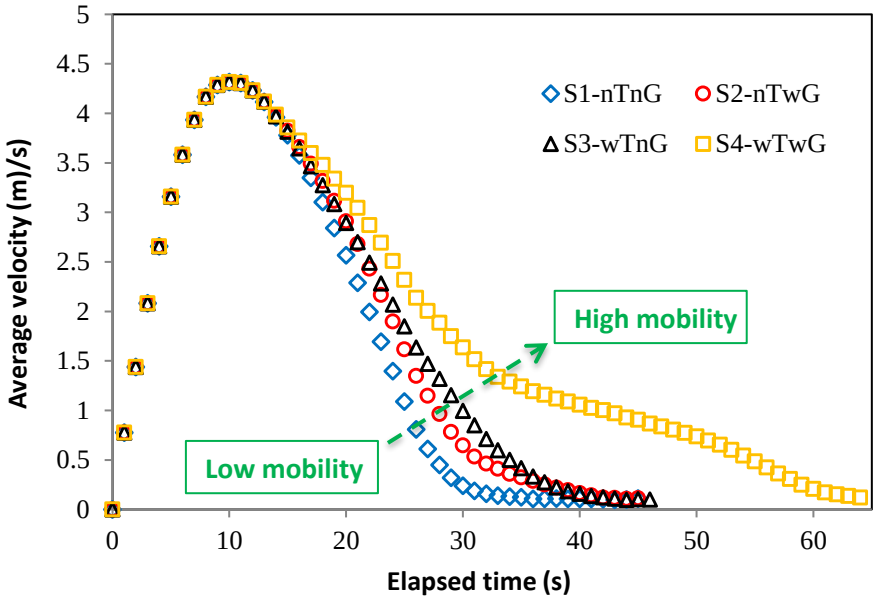

Fig. 11 Average velocity-time curves of the collapsed soil in the four simulation conditions. From S1 to S4 the mobility of the sliding mass increases gradually

6. Conclusions

The run-out process of a rockslide-debris flow in a layered rock slope is studied by an improved finite difference model. Field investigation and numerical simulations on this landslide are conducted to interpret the propagation process, and we obtain the following conclusions.

(1) The run-out process of the Verghereto landslide can be divided into three stages. In the first stage, the landslide detached from the bed rock sliding on the relatively gentle surface in the source zone. Then in the second stage, the landslide descended quickly in the steep slope zone next to the source zone before slumping heavily on the low slope gradient zone, and in the meantime, the volume of the landslide increased by entraining the loose mass on the slope and the rock mass disintegrated quickly. In the final stage, the disintegrated rock mass converged into the gully and transformed into a debris flow, and then the flow propagated along the gully until it stopped at the outlet of the gully.

(2) Simulation results show that the frictional strength change produced by the SFT process probably performs an important role in determining the dynamic characteristics of this landslide.

The run-out behavior and depositional characteristic of the landslide can be correctly simulated if we properly consider this friction strength change of sliding mass. The depth-averaged single-phase model adopted in this study performs well in the simulation of the Verghereto rockslide-debris flow.

(3) Topography may have a dominant impact on the depositional characteristic of the Verghereto landslide. In the landslide area where the slope is relatively steep, the final digital elevation difference shows entrainment. By contrast, in low slope gradient zones, the deposit shows accumulation and deposition. However, bed entrainment should occur on both steep and gentle slopes. Additionally, the existence of a gully channel on the slope could enlarge the run-out distance of the landslide. In the potential rockslides similar to the Verghereto landslide, those with a gully on the slope may pose higher risk to the infrastructures in the outlet of the gully (at slope toe).

Acknowledgement

We would like to thank the anonymous referees for careful reading the manuscript and providing constructive comments to help us improve the quality of this paper. This research is funded by the National Key R&D Program of China (2021YFE0111900), the Fundamental Research Funds for the Central Universities, CHD（300102261507）, and the China Scholarship Council (CSC) – University of Bologna Joint Scholarship (File No. 201806560011).

Reference

Aaron J and McDougall S (2019) Rock avalanche mobility: The role of path material. Engineering Geology 257: 105126. doi: https://doi.org/10.1016/j.enggeo.2019.05.003

Berti M, Cuzzani MG, Vai GB, Landuzzi A, Taviani M and Aharon P (1994) Hydrocarbon-derived imprints in olistostromes of the early serravallian marnoso-arenacea formation, romagna apennines (northern italy). Geo-Marine Letters 14: 192-200. doi: 10.1007/BF01203731

Berti M, Genevois R, Ghirotti M and Tecca PR (1996) Mechanical characteristics and behaviour of a complex formation by landslide investigations and analyses. ISL'96 : International Symposium on landslides (7 ; Trondheim 1996-06-17), A.A. Balkema, Rotterdam, pp

1155-1162.

Bowman ET, Take WA, Rait KL and Hann C (2012) Physical models of rock avalanche spreading behaviour with dynamic fragmentation. Canadian Geotechnical Journal 49: 460-476. doi: 10.1139/t2012-007

Christen M, Kowalski J and Bartelt P (2010) Ramms: Numerical simulation of dense snow avalanches in three-dimensional terrain. Cold Regions Science and Technology 63: 1-14. doi: https://doi.org/10.1016/j.coldregions.2010.04.005

Collins BD and Reid ME (2019) Enhanced landslide mobility by basal liquefaction: The 2014 state route 530 (oso), washington, landslide. GSA Bulletin 132: 451-476. doi: 10.1130/B35146.1

Crosta GB, Frattini P and Fusi N (2007) Fragmentation in the val pola rock avalanche, italian alps. Journal of Geophysical Research: Earth Surface 112. doi: 10.1029/2005JF000455

Cuomo S, Pastor M, Capobianco V and Cascini L (2016) Modelling the space–time evolution of bed entrainment for flow-like landslides. Engineering Geology 212: 10-20. doi: 10.1016/j.enggeo.2016.07.011

Dai Z, Huang Y, Cheng H and Xu Q (2017) Sph model for fluid–structure interaction and its application to debris flow impact estimation. Landslides 14: 917-928. doi: 10.1007/s10346-016-0777-4

Davies TR and McSaveney MJ (2009) The role of rock fragmentation in the motion of large landslides. Engineering Geology 109: 67-79. doi: https://doi.org/10.1016/j.enggeo.2008.11.004

Dufresne A and Geertsema M (2020) Rock slide–debris avalanches: Flow transformation and hummock formation, examples from british columbia. Landslides 17: 15-32. doi: 10.1007/s10346-019-01280-x

Gao G, Meguid MA, Chouinard LE and Zhan W (2021) Dynamic disintegration processes accompanying transport of an earthquake-induced landslide. Landslides 18: 909-933. doi: 10.1007/s10346-020-01508-1

Gao Y, Yin Y, Li B, Feng Z, Wang W, Zhang N and Xing A (2017) Characteristics and numerical runout modeling of the heavy rainfall-induced catastrophic landslide–debris flow at sanxicun, dujiangyan, china, following the wenchuan ms 8.0 earthquake. Landslides 14:

1361-1374. doi: 10.1007/s10346-016-0793-4

Ghaïtanellis A, Violeau D, Liu PLF and Viard T (2021) Sph simulation of the 2007 chehalis lake landslide and subsequent tsunami. Journal of Hydraulic Research: 1-25. doi: 10.1080/00221686.2020.1844814

Guthrie RH, Friele P, Allstadt K, Roberts N, Evans SG, Delaney KB, Roche D, Clague JJ and Jakob M (2012) The 6 august 2010 mount meager rock slide-debris flow, coast mountains, british columbia: Characteristics, dynamics, and implications for hazard and risk assessment. Nat Hazards Earth Syst Sci 12: 1277-1294. doi: 10.5194/nhess-12-1277-2012

Hungr O and Evans SG (2004) Entrainment of debris in rock avalanches: An analysis of a long run-out mechanism. GSA Bulletin 116: 1240-1252. doi: 10.1130/B25362.1

Hungr O, Leroueil S and Picarelli L (2014) The varnes classification of landslide types, an update. Landslides 11: 167-194. doi: 10.1007/s10346-013-0436-y

Hungr O and McDougall S (2009) Two numerical models for landslide dynamic analysis. Computers & Geosciences 35: 978-992. doi: 10.1016/j.cageo.2007.12.003

Iverson RM and Ouyang C (2015) Entrainment of bed material by earth-surface mass flows: Review and reformulation of depth-integrated theory. Reviews of Geophysics 53: 27-58. doi: 10.1002/2013RG000447

Li X, Tang X, Zhao S, Yan Q and Wu Y (2021) Mpm evaluation of the dynamic runout process of the giant daguangbao landslide. Landslides 18: 1509-1518. doi: 10.1007/s10346-020-01569-2

Liang H, He S and Liu W (2020) Dynamic simulation of rockslide-debris flow based on an elastic–plastic framework using the sph method. Bulletin of Engineering Geology and the Environment 79: 451-465. doi: 10.1007/s10064-019-01537-8

Ricci Lucchi Fand Valmori E (1980) Basin-wide turbidites in a miocene, over-supplied deep-sea plain: A geometrical analysis. Sedimentology 27: 241-270. doi: https://doi.org/10.1111/j.1365-3091.1980.tb01177.x

Mangeney CA, Vilotte JP, Bristeau MO, Perthame B, Bouchut F, Simeoni C and Yerneni S (2003) Numerical modeling of avalanches based on saint venant equations using a kinetic scheme. Journal of Geophysical Research: Solid Earth 108. doi:

https://doi.org/10.1029/2002JB002024

McDougall S, Boultbee N, Hungr O, Stead D and Schwab JW (2006) The zymoetz river landslide, british columbia, canada: Description and dynamic analysis of a rock slide–debris flow. Landslides 3: 195. doi: 10.1007/s10346-006-0042-3

McDougall S and Hungr O (2005) Dynamic modelling of entrainment in rapid landslides. Canadian Geotechnical Journal 42: 1437-1448. doi: 10.1139/t05-064

O'Brien JS, Julien PY and Fullerton WT (1993) Two‐dimensional water flood and mudflow simulation. Journal of Hydraulic Engineering 119: 244-261. doi: 10.1061/(ASCE)0733-9429(1993)119:2(244)

Ouyang C, He S and Tang C (2015) Numerical analysis of dynamics of debris flow over erodible beds in wenchuan earthquake-induced area. Engineering Geology 194: 62-72. doi: 10.1016/j.enggeo.2014.07.012

Ouyang C, He S, Xu Q, Luo Y and Zhang W (2013) A maccormack-tvd finite difference method to simulate the mass flow in mountainous terrain with variable computational domain. Computers & Geosciences 52: 1-10. doi: 10.1016/j.cageo.2012.08.024

Pastor M, Haddad B, Sorbino G, Cuomo S and Drempetic V (2009) A depth-integrated, coupled sph model for flow-like landslides and related phenomena. International Journal for Numerical and Analytical Methods in Geomechanics 33: 143-172. doi: 10.1002/nag.705

Sassa K, Nagai O, Solidum R, Yamazaki Y and Ohta H (2010) An integrated model simulating the initiation and motion of earthquake and rain induced rapid landslides and its application to the 2006 leyte landslide. Landslides 7: 219-236. doi: 10.1007/s10346-010-0230-z

Sassa K and Wang Gh (2005) Mechanism of landslide-triggered debris flows: Liquefaction phenomena due to the undrained loading of torrent deposits. In: Jakob M and Hungr O (eds) Debris-flow hazards and related phenomena, Springer Berlin Heidelberg, Berlin, Heidelberg, pp 81-104. doi: 10.1007/3-540-27129-5_5

Shen W, Li T, Li P, Berti M, Shen Y and Guo J (2019) A two-layer numerical model for simulating the frontal plowing phenomenon of flow-like landslides. Engineering Geology 259: 105168. doi: 10.1016/j.enggeo.2019.105168

Shen W, Li T, Li P and Guo J (2018) A modified finite difference model for the modeling of

609 flowslides. Landslides 15: 1577-1593. doi: 10.1007/s10346-018-0980-6
610 Shugar DH, Jacquemart M, Shean D, Bhushan S, Upadhyay K, Sattar A, Schwanghart W, McBride
611 S, de Vries MVW, Mergili M, Emmer A, Deschamps-Berger C, McDonnell M, Bhambri R,
612 Allen S, Berthier E, Carrivick JL, Clague JJ, Dokukin M, Dunning SA, Frey H, Gascoin S,
613 Haritashya UK, Huggel C, Kääb A, Kargel JS, Kavanaugh JL, Lacroix P, Petley D, Rupper S,
614 Azam MF, Cook SJ, Dimri AP, Eriksson M, Farinotti D, Fiddes J, Gnyawali KR, Harrison S,
615 Jha M, Koppes M, Kumar A, Leinss S, Majeed U, Mal S, Muhuri A, Noetzli J, Paul F,
616 Rashid I, Sain K, Steiner J, Ugalde F, Watson CS and Westoby MJ (2021) A massive rock
617 and ice avalanche caused the 2021 disaster at chamoli, indian himalaya. Science 373: 300.
618 doi: 10.1126/science.abh4455
619 Soga K, Alonso E, Yerro A, Kumar K and Bandara S (2016) Trends in large-deformation analysis of
620 landslide mass movements with particular emphasis on the material point method.
621 Géotechnique 66: 248-273. doi: 10.1680/jgeot.15.LM.005
622 Wang FW, Sassa K and Wang G (2002) Mechanism of a long-runout landslide triggered by the
623 august 1998 heavy rainfall in fukushima prefecture, japan. Engineering Geology 63:
624 169-185. doi: https://doi.org/10.1016/S0013-7952(01)00080-1
625 Wu J-H, Lin W-K and Hu H-T (2018) Post-failure simulations of a large slope failure using 3dec:
626 The hsien-du-shan slope. Engineering Geology 242: 92-107. doi:
627 https://doi.org/10.1016/j.enggeo.2018.05.018
628 Xia X and Liang Q (2018) A new depth-averaged model for flow-like landslides over complex
629 terrains with curvatures and steep slopes. Engineering Geology 234: 174-191. doi:
630 https://doi.org/10.1016/j.enggeo.2018.01.011
631 Xing AG, Wang G, Yin YP, Jiang Y, Wang GZ, Yang SY, Dai DR, Zhu YQ and Dai JA (2014)
632 Dynamic analysis and field investigation of a fluidized landslide in guanling, guizhou, china.
633 Engineering Geology 181: 1-14. doi: https://doi.org/10.1016/j.enggeo.2014.07.022
634 Xu Q, Fan X, Huang R, Yin Y, Hou S, Dong X and Tang M (2010) A catastrophic rockslide-debris
635 flow in wulong, chongqing, china in 2009: Background, characterization, and causes.
636 Landslides 7: 75-87. doi: 10.1007/s10346-009-0179-y
637 Xu X, Jin F, Sun Q, Soga K and Zhou GGD (2018) Three-dimensional material point method

modeling of runout behavior of the hongshiyan landslide. Canadian Geotechnical Journal 56: 1318-1337. doi: 10.1139/cgj-2017-0638

Yin Y, Cheng Y, Liang J and Wang W (2016) Heavy-rainfall-induced catastrophic rockslide-debris flow at sanxicun, dujiangyan, after the wenchuan ms 8.0 earthquake. Landslides 13: 9-23. doi: 10.1007/s10346-015-0554-9

Zhang X, Krabbenhoft K, Sheng D and Li W (2015) Numerical simulation of a flow-like landslide using the particle finite element method. Computational Mechanics 55: 167-177. doi: 10.1007/s00466-014-1088-z

Zhang X, Wang L, Krabbenhoft K and Tinti S (2020) A case study and implication: Particle finite element modelling of the 2010 saint-jude sensitive clay landslide. Landslides 17: 1117-1127. doi: 10.1007/s10346-019-01330-4